# Micromechanism of Decrease of Impact Toughness in Coarse-Grain Heat-Affected Zone of HSLA Steel with Increasing Welding Heat Input

R. CAO, J. LI, D.S. LIU, J.Y. MA, and J.H. CHEN

This paper analyzes the micromechanism of decrease of impact toughness with increasing the welding heat input in coarse-grain heat-affected zone (CGHAZ) of a low-alloy high-strength ship-building steel plate. By comparing the microstructures, measuring the extending length of the fibrous crack, identifying the critical event of cleavage fracture, measuring the critical length, and calculating the local cleavage fracture stress $\sigma_f$, and then using the basic principles of the micromechanism of cleavage fracture, this work reveals the essential causes of deteriorated toughness in the CGHAZ of high-strength steel welded joints.

DOI: 10.1007/s11661-015-2916-2


## I. INTRODUCTION

ADVANCED heavy plates of high-strength low-alloy (HSLA) steels with higher strength, enhanced impact toughness and improved weldability have been developed since 1970s. Heavy thickness, extra-width, and extra-length steel plate with yield strength higher than 460 MPa is widely used for ship-building.[1–5] Due to the lower carbon content these steels show less sensitivity to hydrogen-induced cold crack (HICC) and can be welded without preheating, therefore reduce the time and cost of fabrication. However, for these steels, welding is still a critical process, which produces the coarse-grain heat-affected zone (CGHAZ) and deteriorates the property of the welded joint. It was found that CGHAZ had a higher susceptibility to HICC than the weld metal (WM) and the HICC cracking rate decreased notably with the increasing heat input.[6] In most cases, the CGHAZ showed the lowest ductility and toughness,[7–12] which was related to coarsening grain size in the CGHAZ and coarse martensite-austenite (M–A) constituent. Therefore, more studies were concentrated on studying microstructures and properties of the heat-affected zone (HAZ) by varying peak temperatures, heat inputs, and alloy compositions.[7–19] In Reference 12 coarse austenite grain size associated with coarse M–A constituent along grain boundary was revealed as the dominant factor in promoting brittle fracture. The combination of fine prior austenite grain size and smaller M–A constituent was favorable in obtaining high toughness. Good toughness was obtained upon refining the prior austenite grain size in the CGHAZ in the first pass and hence in the intercritical coarse-grain heat-affected zone (ICCGHAZ) in the second pass. Banerjee *et al.*[13] found that compared with the heating rate, the peak temperature of thermal cycle at simulated HAZ of ×80 pipeline steel played a dominant role on final austenite grain size. Zhang and Kannengiesser *et al.*[14] studied the microstructure and hardness in simulated HAZs of micro-alloyed HSLA steels. They found that the peak temperature affected microstructure and hardness, and the heat simulated results were consistent with that of real weld HAZ. In Reference 15 a newly developed high-strength high-toughness steel E690 for offshore structures was studied. It was revealed that a high heat input welding followed by a fast cooling cycle was a promising welding process to improve the efficiency and toughness of offshore steels because it decreased the austenite grain size and residual M–A constituent. Furthermore, the toughness in the CGHAZ decreased with the increasing welding heat input.[16–18] At high heat input, the grain size in CGHAZ could reach more than ten times of the original average values.

Except the effects of peak temperature and heat input on microstructure and properties of CGHAZ, alloy contents have also major effects on microstructure and properties of CGHAZ. In Reference 19 the amount of retained austenite in M–A constituents changed with varying Al contents. The results indicated that appropriate aluminum addition could decrease not only the area fraction but also the size of M–A constituents, which were beneficial for improving the toughness of HAZ.

Although most studies have indicated that CGHAZ had the lowest Charpy toughness and was the weakest part in HAZ, several studies[20,21] claimed that the impact toughness in CGHAZ was higher than that in fine-grain HAZ (FGHAZ)). In Reference 21 the toughness of coarse-grain (CG) specimens which was superior

R. CAO and J.H. CHEN, Professors, J. LI, Graduate, and J.Y. MA, Engineer, are with the State Key Laboratory of Gansu Advanced Processing and Recycling of Non-ferrous Metallic Metals and Key Laboratory of Non-ferrous Metal Alloys of the Ministry of Education, Lanzhou University of Technology, Lanzhou 730050, P.R. China. Contact e-mail: zchen@lut.cn D.S. LIU, Senior Researcher, Manager, is with the Institute of Research of Iron and Steel, Shasteel, Zhangjiagang, 215623 Jiangsu, P.R. China.
Manuscript submitted December 3, 2014.
Article published online April 28, 2015

to that of fine-grain (FG) specimens appeared only in notched specimen due to its high stress triaxiality, by which the specimen was fractured at a lower fracture strain. This strain level was lower than what needed to nucleate the voids by breaking the tiny carbide plates precipitated inside the bainitic laths in CG specimens.

In Reference 22 Liu *et al.* analyzed the relationship between the impact fracture behavior and the microstructures in the CGHAZ of an advanced F460 high-strength steel for ship-building. The low toughness of CGHAZ was attributed to the increase of the effective grain size with the increasing heat input. The present paper based on the principles described in Reference 23 further investigates in depth the micromechanism of the variation of impact toughness in CGHAZ produced with various welding heat inputs.

## II. EXPERIMENTAL

### A. *Material*

F460 steel is a high-strength thermo-mechanical control process (TMCP) steel with low carbon in combination of strengthening elements Cu, Ni, and Cr and modifying elements Nb, V, and Ti. Its normal compositions are listed in Table I.

**Table I. Compositions of Steel F460 (Weight Percent)**

| C | Si | Mn | P | S | Al | Nb + V + Ti | Cu + Ni + Cr |
|---|---|---|---|---|---|---|---|
| 0.062 | 0.23 | 1.47 | 0.008 | 0.002 | 0.040 | 0.094 | 0.60 |

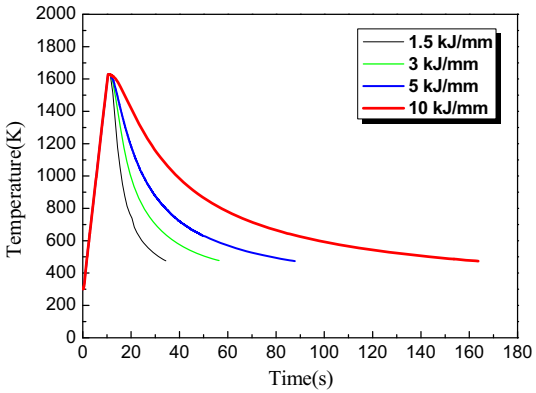


Fig. 1—Simulating heat cycles at four heat input levels.

### B. *Heat Simulated Experiments of Heat-Affected Zone*

10 mm × 10 mm × 75 mm trans-direction (TD) specimens were taken at quarter thickness (1/4) of a 50-mm-thick F460 steel plate. Heat simulated experiments were carried out in a Gleeble-3800 simulator, according to the heat cycle curves shown in Figure 1. These heat cycle curves were calculated for HAZ by the Rykalin formula[24] at four heat input levels *i.e.*, 1.5, 3.0, 5.0, and 10.0 kJ/mm. The specimens were heated at 403 K/s (130 °C/s) to the peak temperature 1623 K (1350 °C), held for 1 second, and then cooled at various cooling rates. The cooling times from 1073 K to 773 K (800 °C to 500 °C) ($t_{8/5}$) were 3.9, 7.7, 12.9, and 25.7 s for the four heat input levels, which are listed in Table II.

### C. *Microstructural Analyses*

The microstructures of heat simulated specimens were observed by optical microscopy (OM) and scanning electron microscopy (SEM). For depicting the prior austenite grains, the specimens were etched by picric acid, and for bainite packets the specimens were etched by the nital solution. To further clearly characterize the grain size and higher degree boundaries, orientation imaging mapping (OIM) electron backscattered diffraction (EBSD) technique was used in the SEM JEOL6500. The SEM was operated at 20 kV. The scan of a 160 $\mu$m × 160 $\mu$m EBSD area was performed using a hexagonal grid with a step size of 0.1 $\mu$m.

### D. *Mechanical Tests*

Tensile tests were carried out by the tester SHIMADZU AG-10T at room temperature (RT) [293 K (20 °C)], 178 K, 168 K, and 77 K (−95 °C, −105 °C, and −196 °C). Special round specimens with a gage size of 5 mm in diameter and 10 mm in length, which just covered the size of simulated CGHAZ, are designed as shown in Figure 2, thus uniform heat-affected regions could be obtained in the tensile gage range.

Charpy V impact tests were carried out using a 450-J instrumented pendulum impact tester for specimens at 293 K, 253 K, 233 K, 213 K, 193 K, 178 K, 168 K, and 77 K (20 °C, −20 °C, −40 °C, −60 °C, −80 °C, −95 °C, −105 °C, and −196 °C). The low temperatures were obtained by controlling the mixture proportion of liquid nitrogen and ethyl alcohol. Standard Charpy V specimens are used, as shown in Figure 3. Load–displacement curves and absorbed energy were measured by the instrumented Charpy V impact tester. A

**Table II. Corresponded Parameters at Different Heat Inputs**

| Heat Input (kJ/mm) | $t_{8/5}$ (s) | Hardness (HV) | Max Size of Austenite Grain ($\mu$m) | Max size of Bainite Packet ($\mu$m) | Transition Temperature $T_k$ [K (°C)] |
|---|---|---|---|---|---|
| 1.5 | 3.9 | 343 | 164 | 56 | 178 (−95) |
| 3 | 7.7 | 319 | 225 | 85 | 213 (−60) |
| 5 | 12.9 | 273 | 282 | 105 | 233 (−40) |
| 10 | 25.7 | 243 | 293 | 132 | 243 (−30) |

typical figure is presented in Figure 4. The areas noted by $E_i$ and $E_p$ characterize the absorbed energy in crack initiation and propagation processes, respectively. The total absorbed energy was designated as the CVN energy. The dynamic yield strength $\sigma_{yd}$ was calculated from the measured dynamic yield load $P_y$ by the following formula.

$$\sigma_{yd} = 2.99\, P_y W/B(W-a)^2, \qquad [1]$$

where $W$ is the height, $B$ is the thickness, and $a$ is the notch depth of the Charpy specimen.

### E. *Observation and Micro-parameter Measurement on Fracture Surface*

The fracture surfaces of broken tensile specimens and Charpy V specimens were observed in detail by SEM Quanta 450 FEG (Field Emission Gun). The sites of crack initiation are identified by tracing back the river pattern strips on the fracture surface as shown in Figure 5. The nature of the second phase particle was clarified by energy dispersive spectrometer (EDS). The relative microscopic parameters were measured for analyzing the micromechanism of fracture. Figure 6 demonstrates the measurements of stretch zone width (SZW), fibrous crack length (SCL), and fracture distance $X_f$. The top part in Figure 6 shows the rough surface of the original notch. The second part demonstrates a stretch zone which is located between red parallel line and blue parallel line and pointed by a longer perpendicular black arrow and noted by SZW. SZW is actually produced by blunting the original notch root and is characterized by slid-induced smooth formless pattern. The third part with fine dimple pattern is the fibrous crack length (SCL), which is located between blue parallel line and yellow parallel line, and pointed by a short red perpendicular arrow. At the bottom of Figure 6, there is the cleavage cracking zone (CCZ) which shows several cleavage facets with river pattern trips on them. The fracture distance $X_f$ is the distance from the site of cleavage crack initiation to the blunted notch tip or the fibrous crack, which is located between yellow parallel line and green parallel line, and pointed by a short blue perpendicular arrow. The SZW, SCL, and cleavage cracking zones present an integrated cracking process. The detailed study can be referred in chapter 3 of Reference 23.

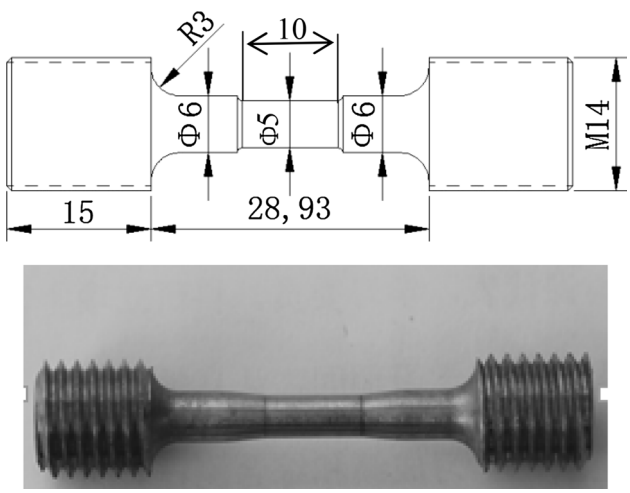


Fig. 2—Dimensions of round tensile specimens.

### F. *Determination of the Critical Event*

The critical event for cleavage fracture[23] is defined by Smith as that 'In developing a realistic physical model of the cleavage process it is of paramount importance to ascertain the nature of the critical event in the formation of a cleavage crack… It is essential to decide if the greatest difficulty in the formation of a crack is its nucleation or whether it occurs at some stage during its growth.'[25] There the critical event is clarified as the stage of greatest difficulty in the formation of the microcrack, and should control the microcracking. The cleavage microcracking process is composed of three stages[23]: the crack nucleation stage, the stage of crack propagation across the particle–grain boundary, and the

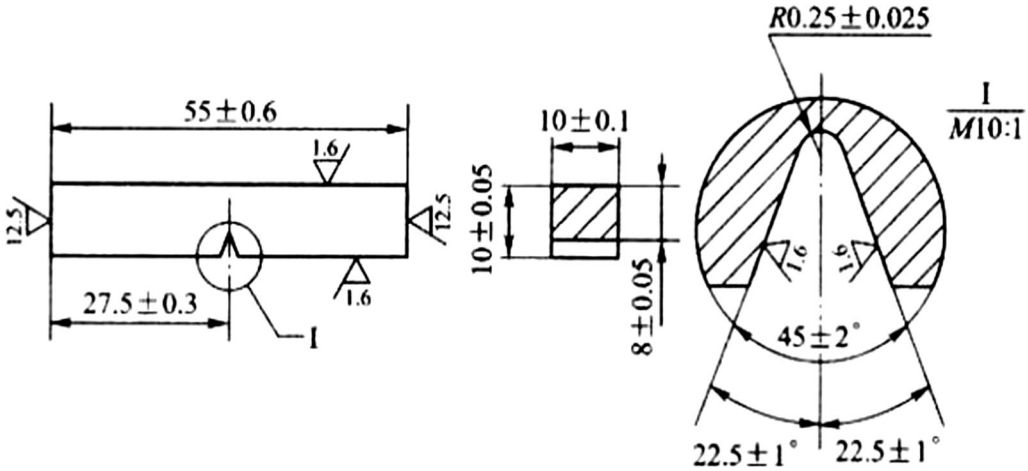


Fig. 3—Dimensions of standard Charpy V specimens.

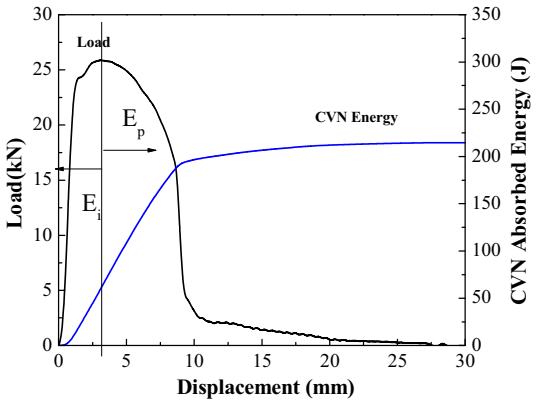


Fig. 4—A typical load–displacement and absorbed energy curves measured by the instrumented Charpy V impact tester.

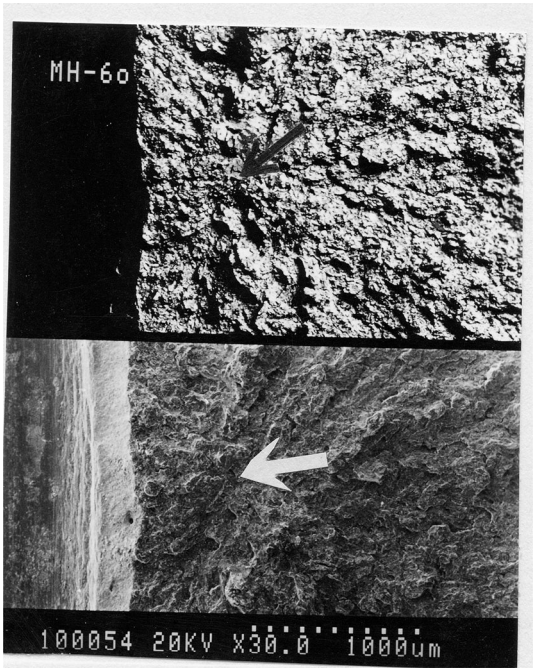


Fig. 5—Identification of the crack initiation site by tracing back the river pattern strips on the fracture surface.[23]

stage of crack propagation across the grain–grain boundary. Each of these three stages is possible to turn into the critical event. Among the three stages, the one which is identified as the critical event will control the cleavage microcracking process. The detailed physical meaning and corresponded study of the critical event in the cleavage microcracking can be referred in Chapter 4 of Reference 23. The critical event was identified by observing the cracks retained in broken specimen. Figure 7 indicates the method to cut the cross section perpendicular to the fracture surface where the retained cracks can be found.

### G. *Finite Element Method (FEM) Calculation*

Figure 8 depicts the FEM model and mesh distribution for the Charpy V specimen using ABAQUS/Explicit code. Power-exponent hardening classic flow curves have been used as material properties.

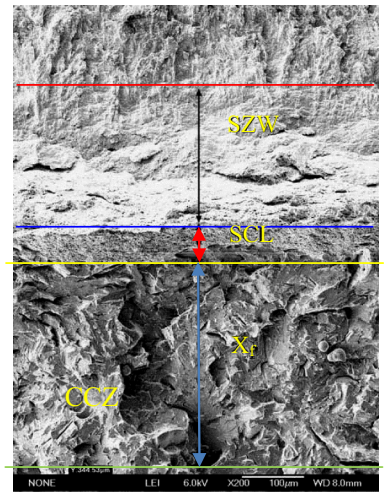


Fig. 6—Measurements of stretch zone width (SZW), fibrous crack length (SCL), and fracture distance ($X_f$) from cleavage fracture initiation origin to the tip of fibrous crack length.

Elements of 8-node linear brick, reduced integration, hourglass control (C3D8R), and 6-node linear triangular prism (C3D6) were taken to form the mesh of the body and the transition region separately. The number of the nodes is 9480, and the number of elements is 6912.

## III. EXPERIMENTAL RESULTS

### A. *Microstructure of Specimens Obtained with Various Simulated Welding Heat Inputs*

Amount papers such as Reference 12 indicated that prior austenite grain size had important effects on final microstructure and properties. For depicting the prior austenite grains, the specimens were etched by picric acid. The prior austenite grains in specimens simulated with heat inputs of 1.5, 3.0, 5.0, and 10.0 kJ/mm are shown in Figure 9. The sizes of the prior austenite grains are measured as the average value of the two lengths measured by the two arrows perpendicular to each other in Figure 9. Figure 10 represents the corresponding proportion distributions of prior austenite grain sizes in CGHAZ. The coarsest austenite grain sizes in specimens with welding heat inputs of 1.5, 3.0, 5.0, and 10.0 kJ/mm are 164, 225, 282, and 293 $\mu$m, respectively (listed in Table II).

For depicting the sizes of bainite packets, the specimens were etched by the nital solution. Figure 11 exhibits the bainite packets observed in specimens simulated with the four heat inputs. In Figure 11, the red arrows have also been denoted to show the measurements of bainite packets.

The measured values of the Vickers hardness HV are 343, 319, 273, and 243, respectively (listed in Table II). By observing the microstructural morphologies shown in Figure 11 and comparing the Vickers hardness HV, the microstructures produced in specimens with various

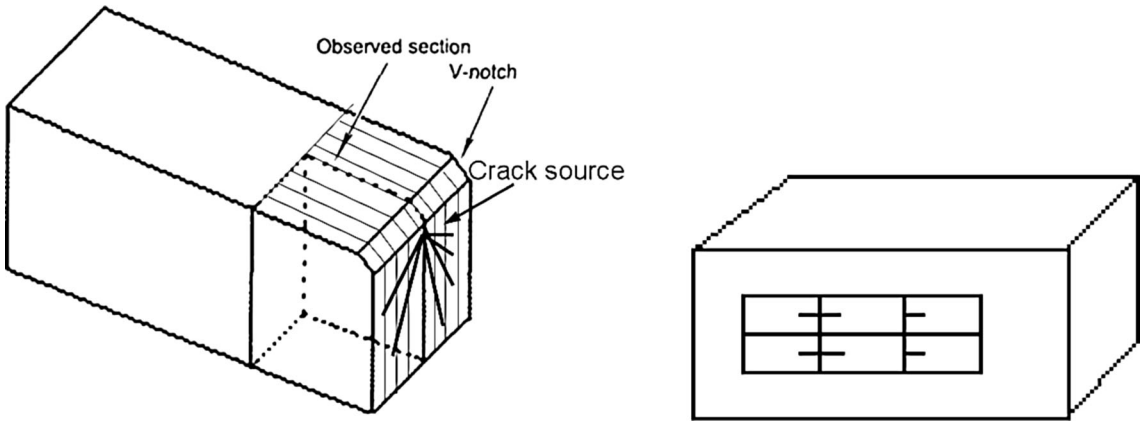


Fig. 7—Cross section perpendicular to the fracture surface for revealing the retained cracks which identify the critical event of cleavage fracture.[23]

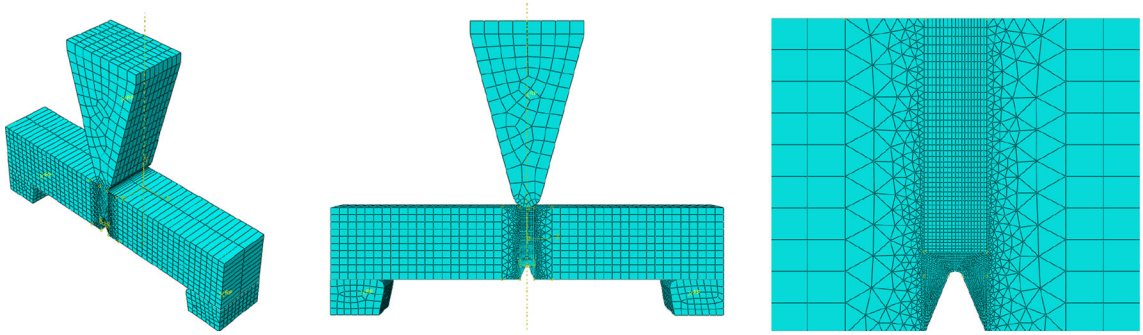

Fig. 8—FEM model and mesh distribution for a Charpy V specimen.

heat inputs are classified as follows: for the specimen with heat input of 1.5 kJ/mm, the microstructural phase is mainly the fine lath martensite mixed with some lath bainite. For the specimen with the heat input of 3.0 kJ/mm, the microstructural phases are the mixture of the fine lath martensite and the fine lath bainite. The microstructural phases for the specimens with 5.0 and 10.0 kJ/mm heat inputs are the mixture of lath bainite and granular bainite. With the increasing heat input, granular bainite increases, and for the specimen with the heat input of 10.0 kJ/mm the granular bainite dominates the microstructure in Figure 11(d).

Figure 12 represents the corresponding proportion distributions of bainite packet sizes in CGHAZ. The coarsest bainite packet sizes in specimens simulated with heat inputs of 1.5, 3.0, 5.0, and 10.0 kJ/mm are 56, 85, 105, and 132 $\mu$m, respectively (listed in Table II). Thus, with the increasing heat input in conjunction with the coarsening of the prior austenite grains, the sizes of the bainite packets increase.

Figure 13 depicts the distributions of misorientation angles measured in the EBSD map in CGHAZ of specimens with the four heat inputs. Figure 14 exhibits the typical EBSD maps showing the higher degree (>15 deg) grain (or packet) boundaries in specimens with heat input of (a) 1.5 kJ/mm, (b) 3.0 kJ/mm, (c) 5.0 kJ/mm, and (d) 10.0 kJ/mm. From Figures 13 and 14, the trend of raising the proportion of the high degree boundaries by decreasing the heat input is clarified.

### B. *Results of Tensile Tests*

Figure 15 plots the variation of the yield strength, ultimate strength, and reduction of fracture area against the temperature for heat simulated specimens. From Figure 15, the yield strength and ultimate strength decrease with the increasing heat input and the test temperature. The reduction of fracture area decreases with the increasing heat input and the decreasing test temperature.

### C. *Impact Toughness and Load–Displacement Curve*

Figure 16 displays the impact toughness transition curves measured in specimens with welding heat input of 1.5, 3.0, 50, and 10.0 kJ/mm. The transition temperature $T_k$ is defined as the temperature where the toughness equals the half value of the sum of the values on the upper shelf and lower shelf, and it characterizes the transition of ductile rupture to the brittle cleavage fracture. For specimens with welding heat inputs of 1.5, 3.0, 5.0, and 10.0 kJ/cm, the values of $T_k$ are about 178 K, 213 K, 233 K, and 243 K(−95 °C, −60 °C, −40 °C, and −30 °C). respectively (listed in Table II).

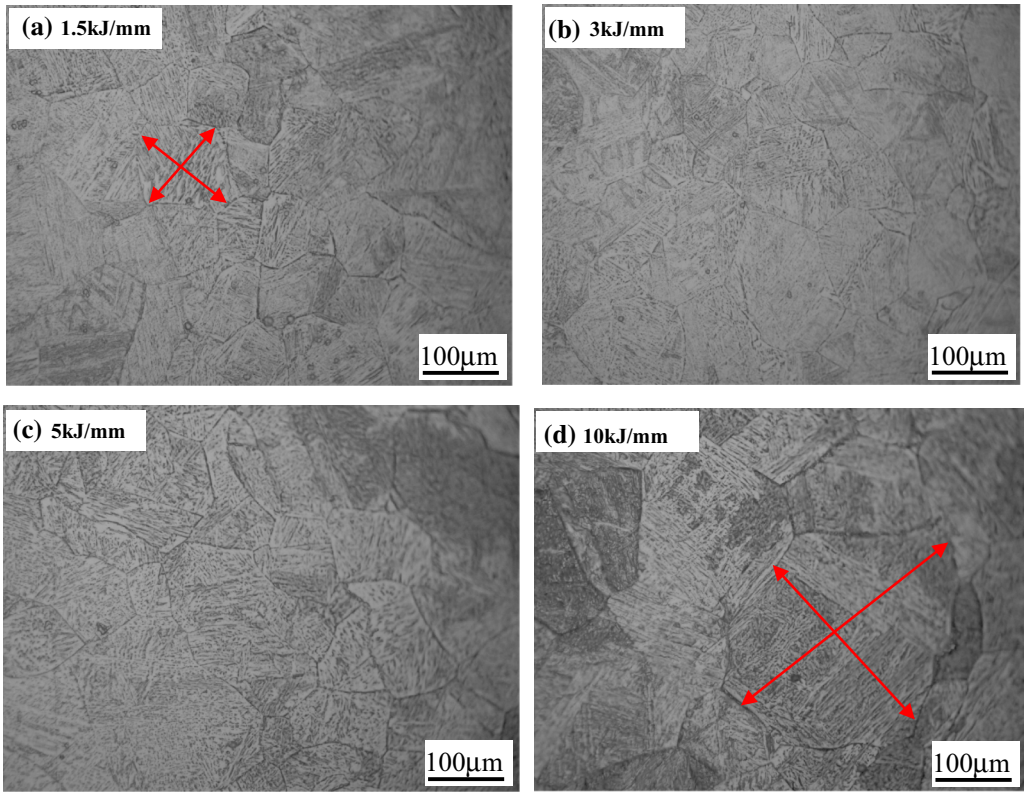


Fig. 9—The prior austenite grains in the coarse-grain HAZ (CGHAZ) of specimens with heat input of (*a*) 1.5 kJ/mm, (*b*) 3 kJ/mm, (*c*) 5 kJ/mm, (*d*) 10 kJ/mm depicted by picric acid etching.

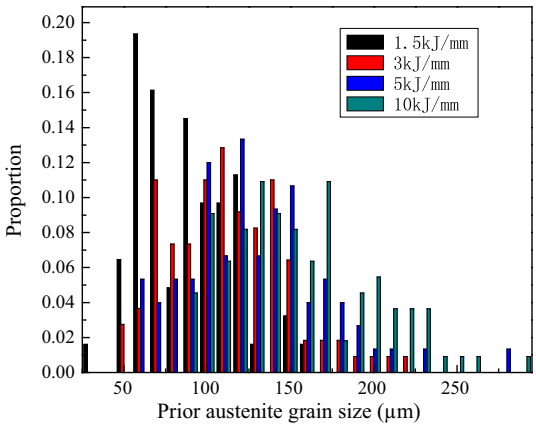


Fig. 10—Distributions of prior austenite grains in the coarse-grain HAZ (CGHAZ) of specimens with heat input of (*a*) 1.5 kJ/mm, (*b*) 3 kJ/mm, (*c*) 5 kJ/mm, (*d*) 10 kJ/mm.

Thus, the toughness transition temperatures rise with the increasing welding heat input. It means that the toughness at a transition temperature decreases with the increasing welding heat inputs.

Figure 17 depicts the load–displacement curves measured by instrumented Charpy V tester at 193 K (−80 °C) for specimens with various welding heat inputs. Apparently, the maximum fracture loads, the crack initiation energy, the crack propagation energy, and the total impact energy all decrease with the increasing welding heat input. The energy for fibrous crack propagation decreases apparently with the increasing heat input from 1.5 to 3.0 kJ/mm. In specimens with heat input of 5.0 and 10.0 kJ/mm, no preceding fibrous crack propagation processes are observed, and only crack blunting processes are produced. It means that crack initiation energy dominates the total energy for Charpy specimens with welding heat input of 5.0 and 10.0 kJ/mm.

### D. *Observation of the Fracture Surface of Broken Charpy V Impact Specimens*

Figures 18 through 20 demonstrate the fracture surfaces of Charpy V specimens fractured at RT [293 K (20 °C)], 193 K (−80 °C), and at 77 K (−196 °C), respectively. The fracture mode is ductile rupture with dimple pattern for all welding heat inputs at RT. With the increasing welding heat input, the width and depth of the dimples seem to decrease; however, no significant variation can be distinguished. At the transition temperature of 193 K (−80 °C), before the initiation of cleavage cracking, a preceding fibrous crack length (SCL) zone is found in specimens with 1.5 and 3.0 kJ/mm welding heat inputs, as shown in Figure 19. In specimens with 5.0 kJ/mm and 10.0 kJ/mm welding heat inputs, only a narrow SZW is developed before cleavage cracking. At 77 K (−196 °C) of lower shelf stage, all specimens were suddenly fractured by brittle cleavage fracture mode as shown in Figure 20. But with the increasing welding heat inputs, the area of cleavage

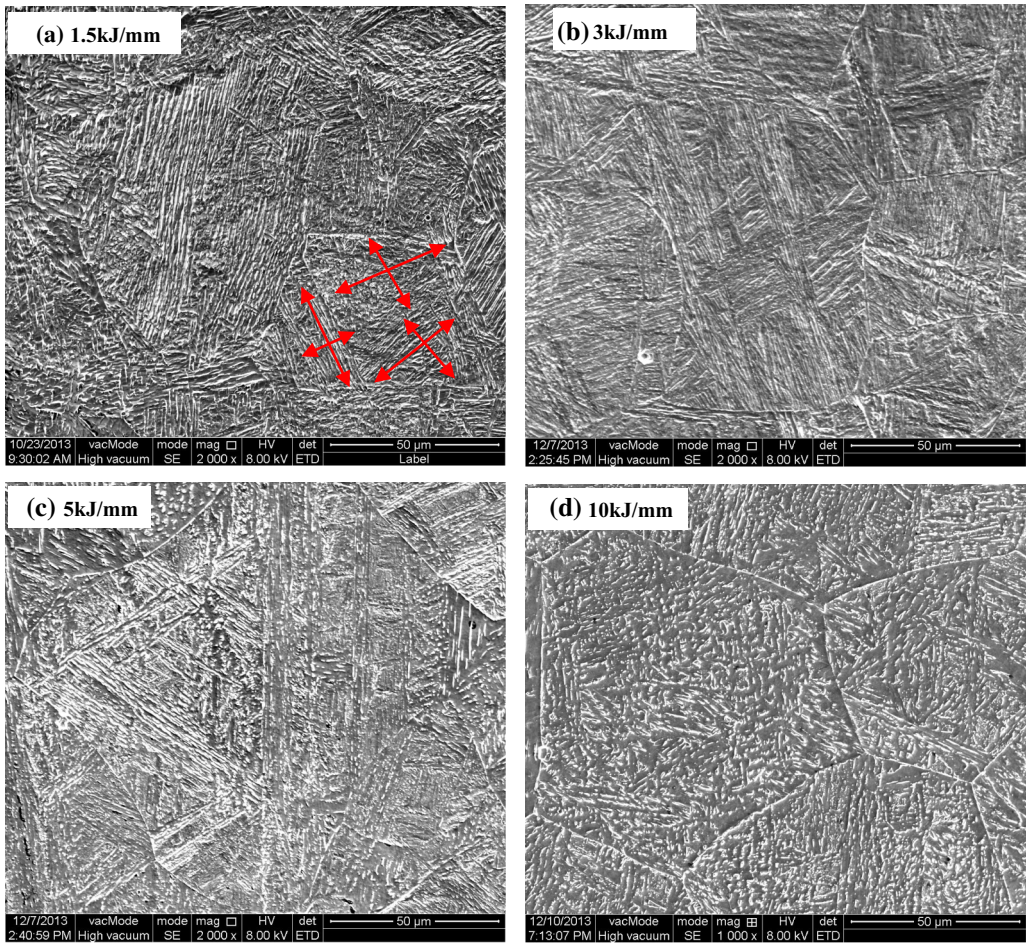


Fig. 11—The bainite (some martensite in (*a*)) packets in the coarse-grain HAZ (CGHAZ) of specimen with heat input of (a) 1.5 kJ/mm, (*b*) 3 kJ/mm, (*c*) 5 kJ/mm, (*d*) 10 kJ/mm depicted by nital etching.

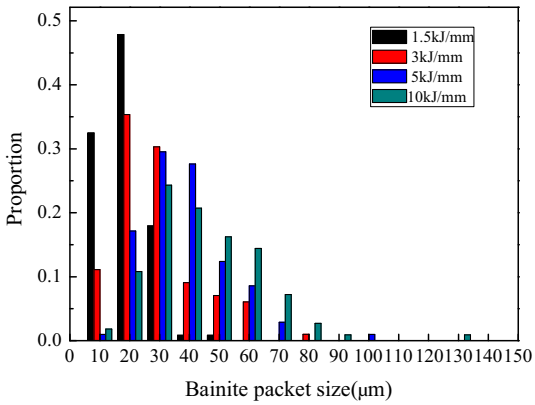


Fig. 12—Distributions of bainite packets in the coarse-grain HAZ (CGHAZ) of specimens with heat input of (*a*) 1.5 kJ/mm, (*b*) 3 kJ/mm, (*c*) 5 kJ/mm, (*d*) 10 kJ/mm.

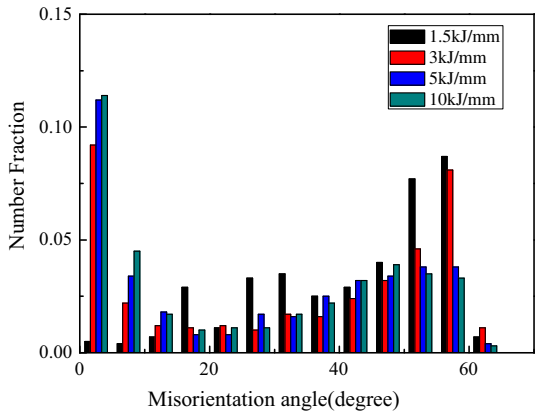


Fig. 13—Distributions of misorientation angles measured in the EBSD map in the coarse-grain HAZ (CGHAZ) of specimens with heat input of (*a*) 1.5 kJ/mm, (*b*) 3 kJ/mm, (*c*) 5 kJ/mm, (*d*) 10 kJ/mm.

fracture facets around the cleavage fracture initiation sites increases. Based on the above observations on fracture surfaces, one can see that the observed SZW zone and the fibrous crack length (SCL) are consistent with that expected by the load–displacement curves in Figure 17. Statistic results of measurements are drawn as in Figure 21. One can see that the total lengths of SZW plus SCL increase with raising the test temperature for all specimens with various welding heat inputs. The energy absorbed in Charpy tests is enhanced with the increase of

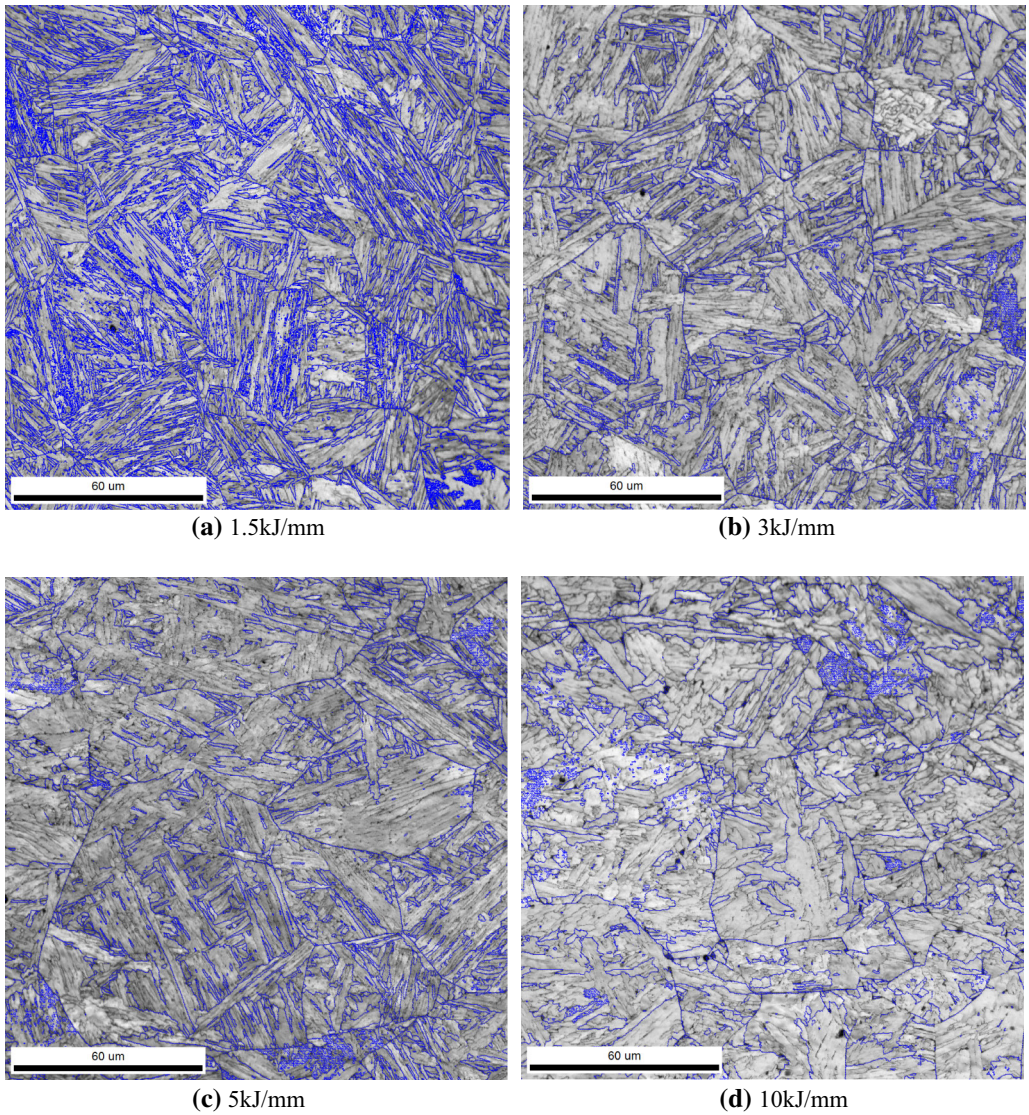


**(a)** 1.5kJ/mm **(b)** 3kJ/mm

**(c)** 5kJ/mm **(d)** 10kJ/mm

Fig. 14—Typical EBSD maps show the higher degree (>15 deg) grain (or packet) boundaries in specimens with heat input of (*a*) 1.5 kJ/mm, (*b*) 3 kJ/mm, (*c*) 5 kJ/mm, and (*d*) 10 kJ/mm.

the SZW plus SCL as depicted in Figure 22. Figure 23 shows the variation of the crack initiation energy with the increase of the SZW. The increasing rate of the crack initiation energy is 0.26 J per unit SZW. Figure 24 shows the variation of the crack propagation energy with the increase of the fibrous crack length (SCL). The increasing rate of the crack propagation energy is 0.056 J per unit SCL. Although the rate of energy rise for unit SZW is much higher than that for unit SCL, however, by comparing Figures 23 and 24, the much longer SCL offsets this superiority and contributes the dominant absorbed energy. In Figures 22 and 24, all experimental points are measured at various temperatures for specimens with various welding heat inputs; therefore, the near-linear relationship between the impact energy and the SCL means the absorbed energy for unit length extension of the fibrous crack (unit SCL) is the same for all specimens tested at various temperatures and with various welding heat inputs. As a result, the total crack propagation energy measured in the transition temperature region is mainly determined by the length of the fibrous crack extended. For all specimens, the maximum of the SZW is limited to about 200 to 500 $\mu$m and the corresponding crack initiation energy is about 40 to 60 J. When test temperature is higher, the fibrous crack is initiated and propagated and the crack propagation energy dominates the total impact energy. In this case, the total impact energy is decided by the extended length of the fibrous crack.

### E. *Cleavage Fracture Distance and the Nature of the Crack Initiation Particle*

The cleavage fracture distance $X_f$ is defined as the distance from the site of cleavage crack initiation to the blunted notch tip or the fibrous crack (if produced) tip. $X_f$ is identified using the method indicated by Figure 5 and is measured as shown in Figure 6. The nature of the

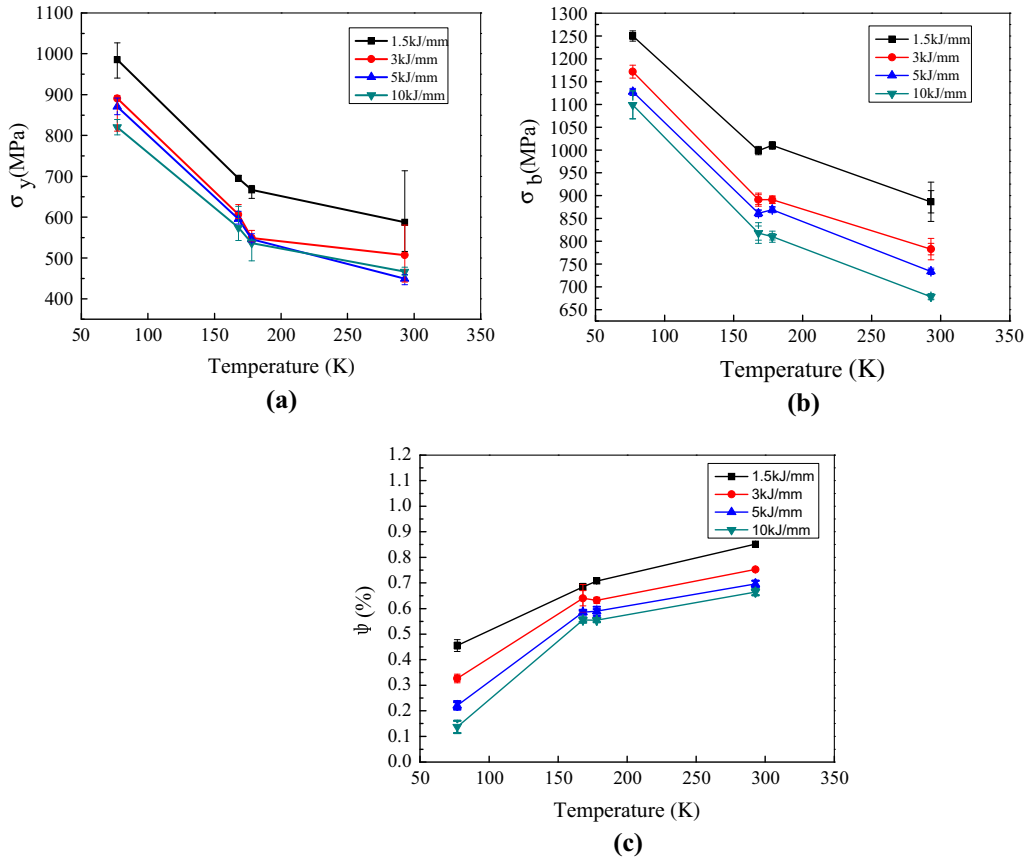


Fig. 15—Variations of (*a*) yield strength $\sigma_y$, (*b*) ultimate strength $\sigma_b$, and (*c*) reduction of fracture area ($\Psi$) with temperature in heat simulated specimens with welding heat inputs of 1.5, 3, 5, and 10 kJ/mm.

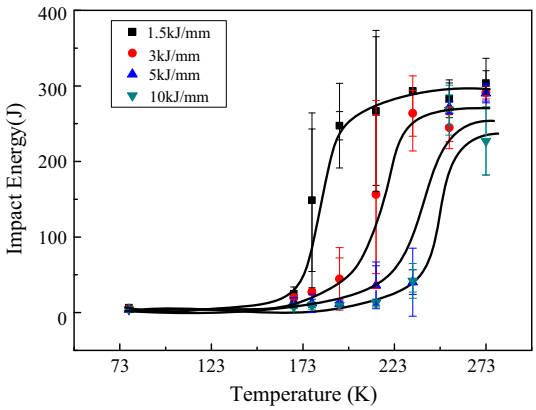


Fig. 16—Impact toughness transition curves measured in specimens with welding heat inputs of 1.5, 3, 5, and 10 kJ/mm.

particle is identified by the EDS. Figure 25 depicts a particle initiating the cleavage cracking. The EDS analyzed result is listed in Table III, which clarifies the cleavage fracture initiation origin being an inclusion particle of CaO, CaS, MnO, and MnS.

## F. *Critical Event for Cleavage Fracture*

The critical event for cleavage fracture, which was clarified as the stage of greatest difficulty during the crack initiation and propagation,[23] is identified by observing the cracks retained in broken specimen as indicated by Figure 7. Figure 26(a) exhibits the packet-sized crack retained in specimen with welding heat input of 1.5 kJ/mm. The retained crack is constrained in a bainite packet and its extension is stopped at the bainite boundaries. Thus, the critical event for cleavage fracture is identified as the propagation of the packet-sized crack. Figure 27 shows the measurements of sizes of retained cracks and bainite packets. Appreciable relationship between the sizes of the retained cracks and the bainite packets supports this identification. The maximum packet size was measured as 56 $\mu$m. Figures 26(b) through (d) demonstrate similar results for specimens with welding heat input of 3.0, 5.0, and 10.0 kJ/mm. All observations proved that the critical event for cleavage fracture was the propagation of the bainite packet-sized crack. The maximum bainite packet sizes were measured as 85, 105, and 132 $\mu$m for specimens with welding heat input of 3.0, 5.0, and 10.0 kJ/mm, respectively (all listed in Table II).

## G. *Results of FEM Calculation*

Figure 8 shows the FEM model and mesh distribution for a Charpy V specimen. Using the hardening model with dynamic yield strength $\sigma_{yd}$, the distribution curves of stress, strain, and stress triaxiality ahead of the notch at 77 K (−196 °C) were calculated and are

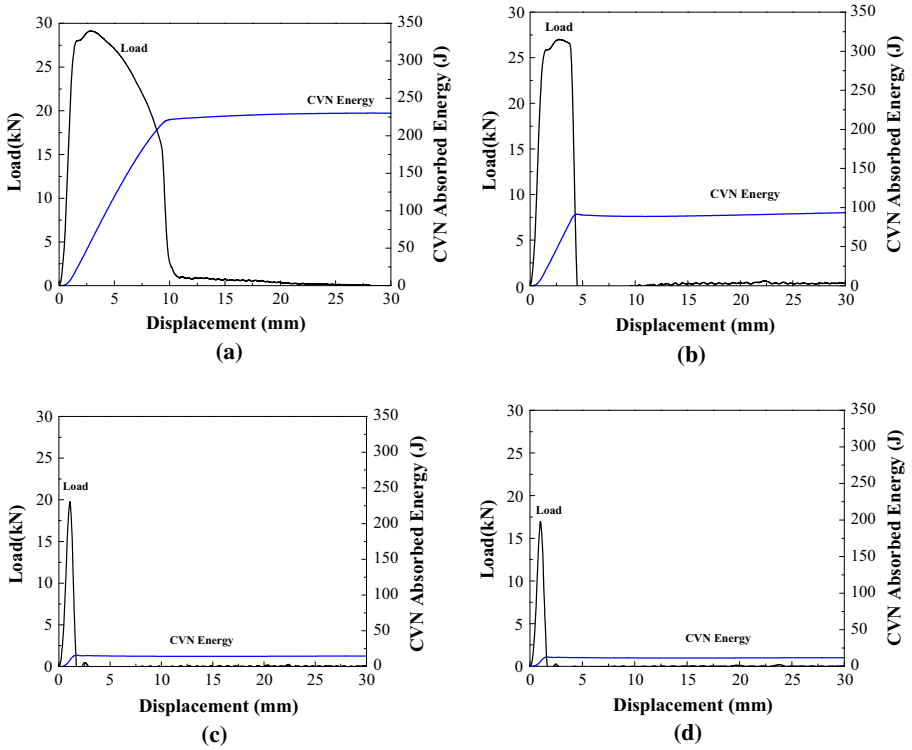


Fig. 17—Load–displacement curves measured by instrumented Charpy V tester at 193 K (−80 °C) for specimens with welding heat input of (*a*)1.5 kJ/mm, (*b*) 3 kJ/mm, (*c*) 5 kJ/mm, and (*d*) 10 kJ/mm.

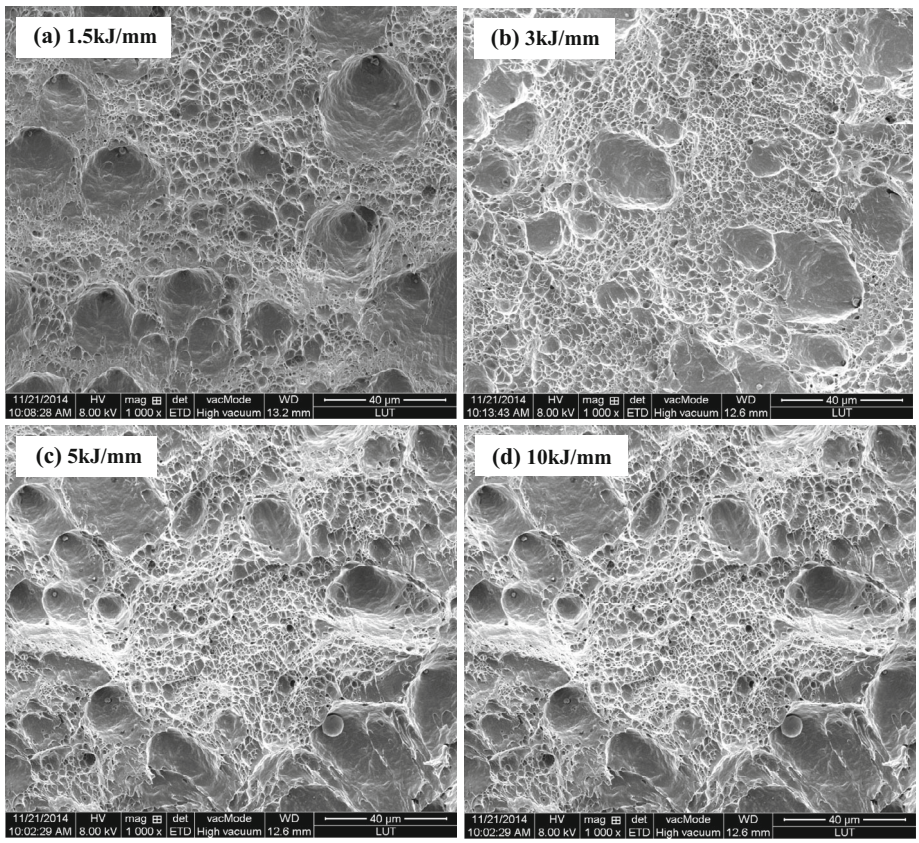


Fig. 18—Fracture surfaces of simulated Charpy V specimens with welding heat input of (*a*) 1.5 kJ/mm, (*b*) 3 kJ/mm, (*c*) 5 kJ/mm, and (*d*) 10 kJ/mm fractured at room temperature [293 K (20 °C)].

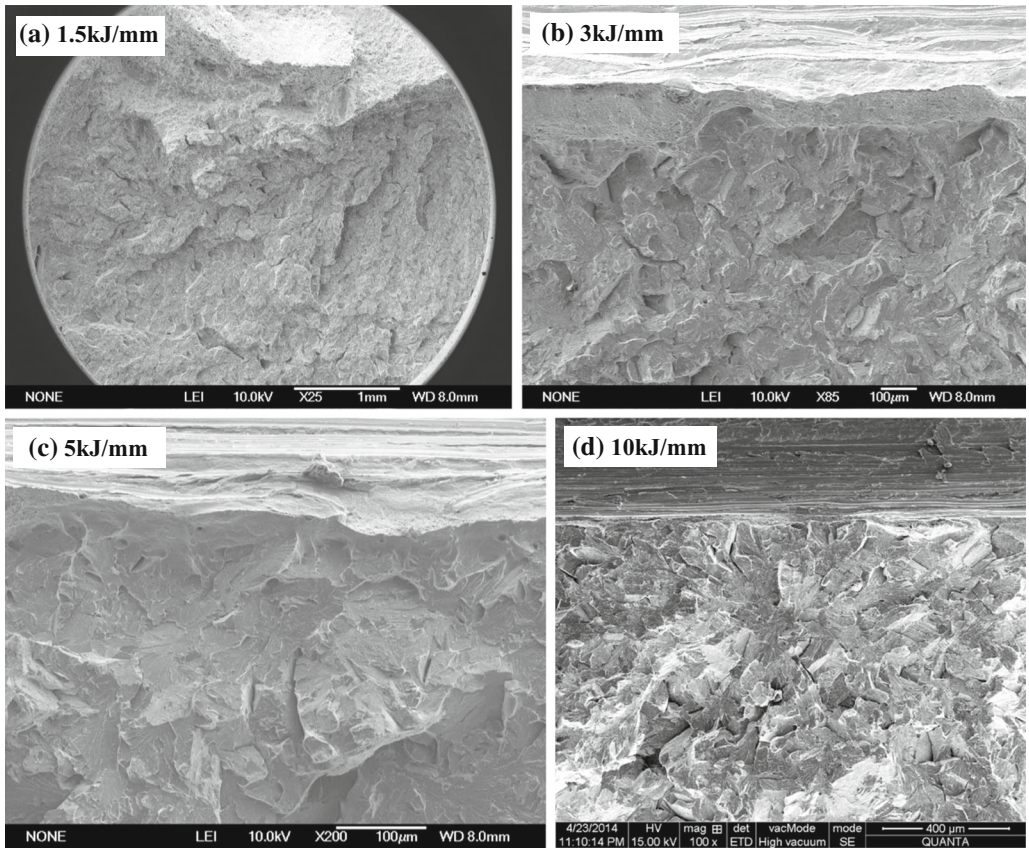


Fig. 19—Fracture surfaces of Charpy V specimens with welding heat input of (*a*) 1.5 kJ/mm (*b*) 3 kJ/mm, (*c*) 5 kJ/mm, (*d*) 10 kJ/mm fractured at 193 K (−80 °C).

displayed in Figure 28. Putting the fracture distance $X_f$ on the abscissa and drawing a vertical line from it, the corresponding values of ordinates on the curves of stress, strain, and stress triaxiality are taken as the local cleavage fracture stress $\sigma_f$, the fracture strain $\varepsilon_{pc}$, and the critical stress triaxiality $T_c$. The measured values of the micro-parameters are listed in Table IV. From the measured $\sigma_f$ and the half length $a_c$ of the cleavage facet area around the crack initiation site by the following well-known Formula [2], the effective surface energy $\gamma$ can be calculated. The values of calculated $\gamma$ are also listed in Table IV

$$\sigma_f = \sqrt{2E\gamma/\pi(1-\nu^2)a_c}. \qquad [2]$$

As mentioned in part *F*, the critical event for cleavage fracture is the propagation of a bainite packet-sized crack. The values of $a_c$ in the above formula should be compatible with the half size of the critical event length, *i.e.*, the half size of the bainite packet-sized crack. The values of $a_c$ listed in Table IV, *i.e.*, 23.4, 34.3, 54.9, and 67.7 $\mu$m, are close to the values of the half sizes of the maximum bainite packets (listed in Table II), *i.e.*, 56/2 = 28, 85/2 = 42.5 $\mu$m. 105/2 = 52.5, and 132/2 = 66 $\mu$m for specimens with various welding heat inputs. Thus, these facts further prove that the critical event for cleavage fracture is the propagations of the packet-sized crack. For further identifying this idea, Figure 29 plots local cleavage fracture stress $\sigma_f$ against the square root of the half maximum size of bainite packet. The slope of the line characterizes the effective surface energy $\gamma$ and the measured values of $\gamma$ are close to the values listed in Table IV. These results further identify the maximum size of the bainite packet is the length of the critical event.

## IV. DISCUSSION

Based on the above experimental results, analyses are carried out on the effects of welding heat inputs on the impact toughness measured in the upper shelf, transition, and lower shelf temperature regions of the toughness transition curves shown in Figure 16.

### A. *The Fracture Mechanism and the Toughness in the Upper Shelf Region*

The micromechanism of fracture on the upper shelf is the ductile rupture[23] in dimple pattern as shown in Figure 18. The mechanism of the global fracture is the extension of the microcracks formed by the primary voids (dimples on fracture surface), which nucleate and grow until impingement resulting in coalescence and final rupture. In the investigated steel, most second phase particles which initiate the dimples and cleavage

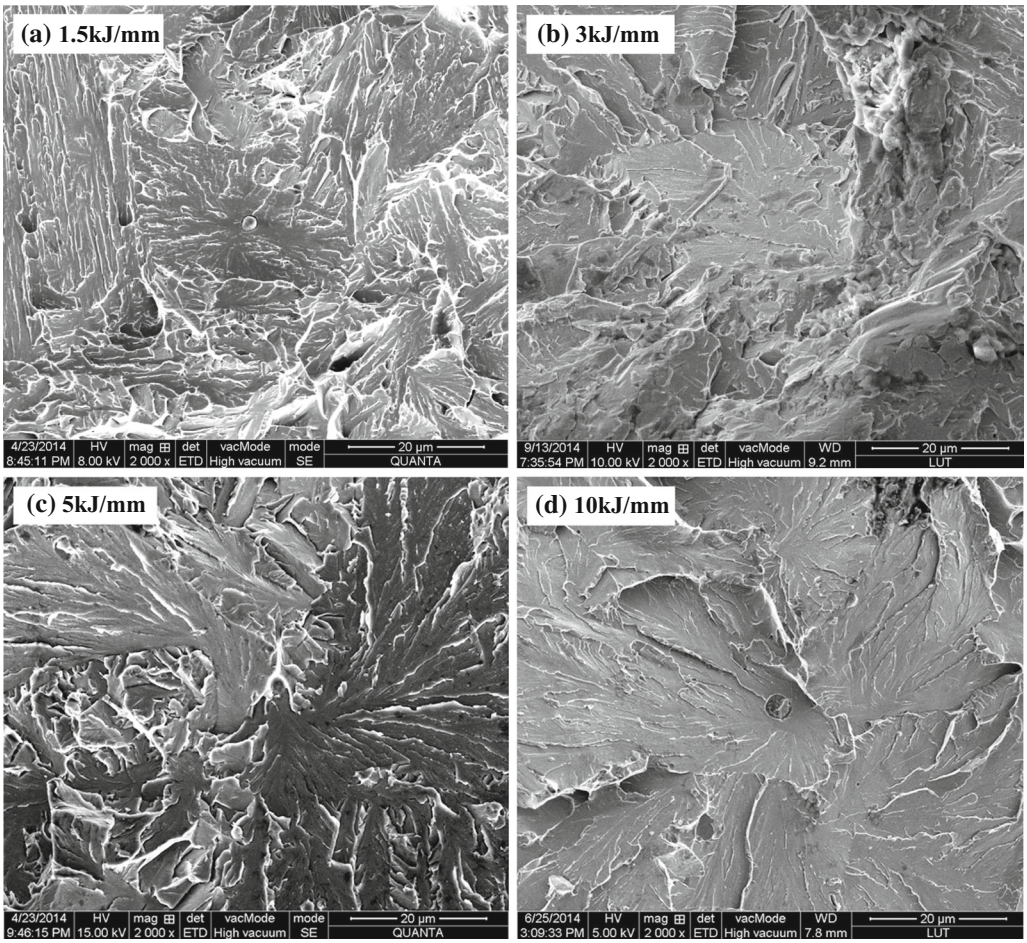


Fig. 20—Fracture surfaces of Charpy V specimens with welding heat inputs of (*a*) 1.5 kJ/mm, (*b*) 3 kJ/mm, (*c*) 5 kJ/mm, (*d*) 10 kJ/mm fractured at 77 K (−196 °C).

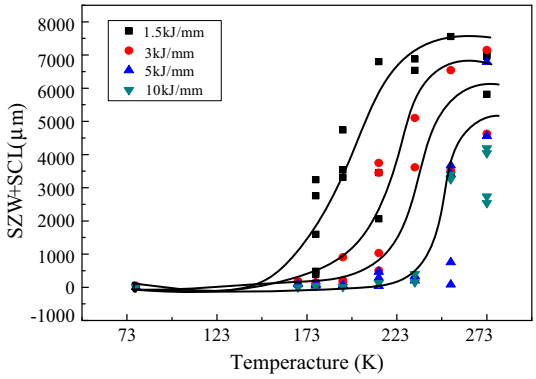


Fig. 21—Stretch zone width (SZW) plus fibrous crack length (SCL) measured at various temperatures in specimens with various welding heat input.

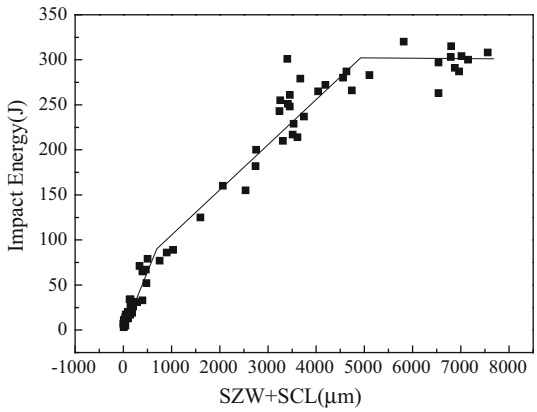


Fig. 22—Plots of the impact energy with stretch zone width (SZW) plus fibrous crack length (SCL) measured at various temperatures in specimens with various welding heat input.

fracture are the non-metallic inclusion as seen in Figure 25. The toughness in the upper shelf region is determined by the density of the brittle inclusion particles and the plasticity of the matrix. As seen in Figure 16, toughness on the upper shelf decreases with the increasing welding heat inputs. This is reasonable because the matrix plasticity decreases (Figure 15(c)) due to the increase of the grain size with the increasing welding heat inputs.

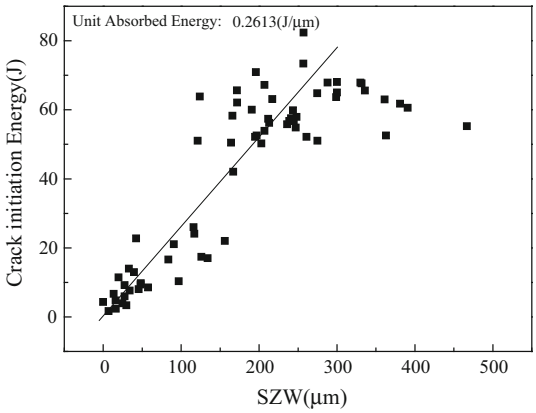


Fig. 23—Variation of the crack initiation energy with the increase of the stretch zone width (SZW) measured at various temperatures in specimens with various welding heat input.

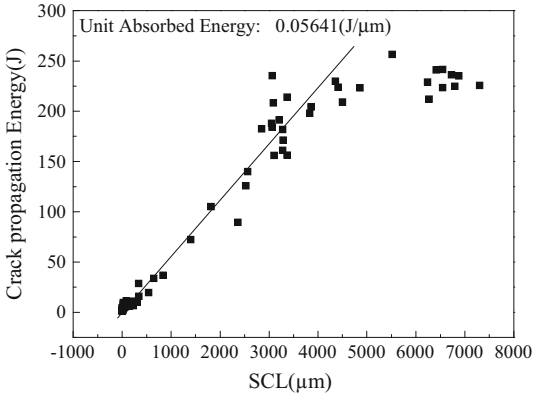


Fig. 24—Variation of the crack propagation energy with the increase of the fibrous crack length (SCL).

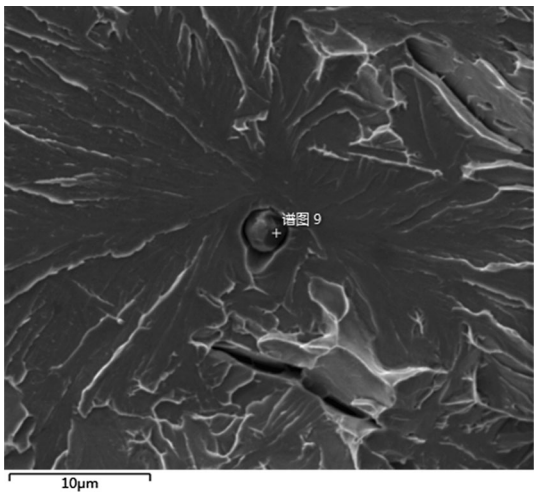


Fig. 25—A particle initiating the cleavage cracking.

### B. *The Fracture Mechanism and the Toughness in the Lower Shelf Region*

Figure 20 depicts the fracture surfaces of specimens with four different welding heat inputs fractured at 77 K (−196 °C). From Figure 20, in the lower shelf region, global fracture occurs in the fully cleavage fracture mode which is essentially different from that of the upper shelf region. The critical event for cleavage fracture in a notched specimen is the propagation of a ferrite grain (or a bainite packet)-sized crack.[23] The global fracture occurs once the cleavage microcracking is triggered, which is controlled by criteria

$$\sigma_{yy} \geq \sigma_f, \qquad [3]$$

where $\sigma_{yy}$ is the normal stress ahead of the notch root which is intensified from $\sigma_y$ through the formula $\sigma_{yy} = Q\sigma_y$. At cleavage cracking, the stress intensification factor $Q = \sigma_{yy}/\sigma_y$ evolves to the critical value $Q_c = \sigma_f/\sigma_y$. In case of impact loading $Q_c = \sigma_f/\sigma_{yd}$, $\sigma_{yd}$ is the dynamic yield strength. The higher $Q_c$ means that more plastic strain needs to be produced to intensify the normal stress $\sigma_{yy}$ to $\sigma_f$. In C-Mn steels, the grain size (the packet size for the bainitic steel) puts a decisive effect on the global fracture toughness by determining both the yield stress $\sigma_y$ and the local fracture stress $\sigma_f$ and determining the size of critical event. The finer the grain sizes (or packet size for the bainite steel), the higher the critical stress intensification factor $Q_c = \sigma_{yy}/\sigma_y = \sigma_f/\sigma_y$ is needed and the higher is the toughness. As revealed in Figures 26 and 27, heat simulated specimens with heat inputs of 1.5, 3.0, 5.0, and 10.0 kJ/mm have the coarsest bainite packets and the maximum retained crack sizes of 56, 85, 105, and 132 $\mu$m, respectively. Correspondingly, the measured values of $\sigma_f$ (listed in Table IV) are 1916, 1567, 1300, and 1104 MPa and the values of critical values of the stress intensification $Q_c = \sigma_f/\sigma_y$ are 1.61, 1.43, 1.29, and 1.23. These results indicated that with the increasing welding heat input the bainite packet sizes increase, which decrease $\sigma_f$ and $Q_c$. The measured $\sigma_f$ and the area of the cleavage facets surrounding the crack initiation sites support the calculated values of the effective surface energy $\gamma$ fluctuating in a reasonable range (shown in Table IV). It means that the resistances within the bainite packets are similar for all specimens. The different values of $\sigma_f$ are caused only by the different sizes of the packets presented as '$a_c$' in Formula [2].

As displayed in Figure 16, although the lowest toughness values in the lower shelf region for various specimens are almost the same, however, the transition start temperature where the toughness starts to rise is different. These are 138 K, 163 K, 193 K, and 213 K (−135 °C, −110 °C, −80 °C, and −60 °C) for specimens with heat inputs of 1.5, 3.0, 5.0, and 10.0 kJ/mm. The rise of the transition start temperature means the

**Table III. The Main Chemical Compositions of a Second Phase Particle in Fig. 25 (Weight Percent)**

| Ca | Mn | S | O | Al | Mg | Fe | Phases |
|---|---|---|---|---|---|---|---|
| 32.5 | 5.8 | 34.2 | 17.1 | 5.1 | 0.7 | 4.3 | CaO, CaS, MnO, MnS |

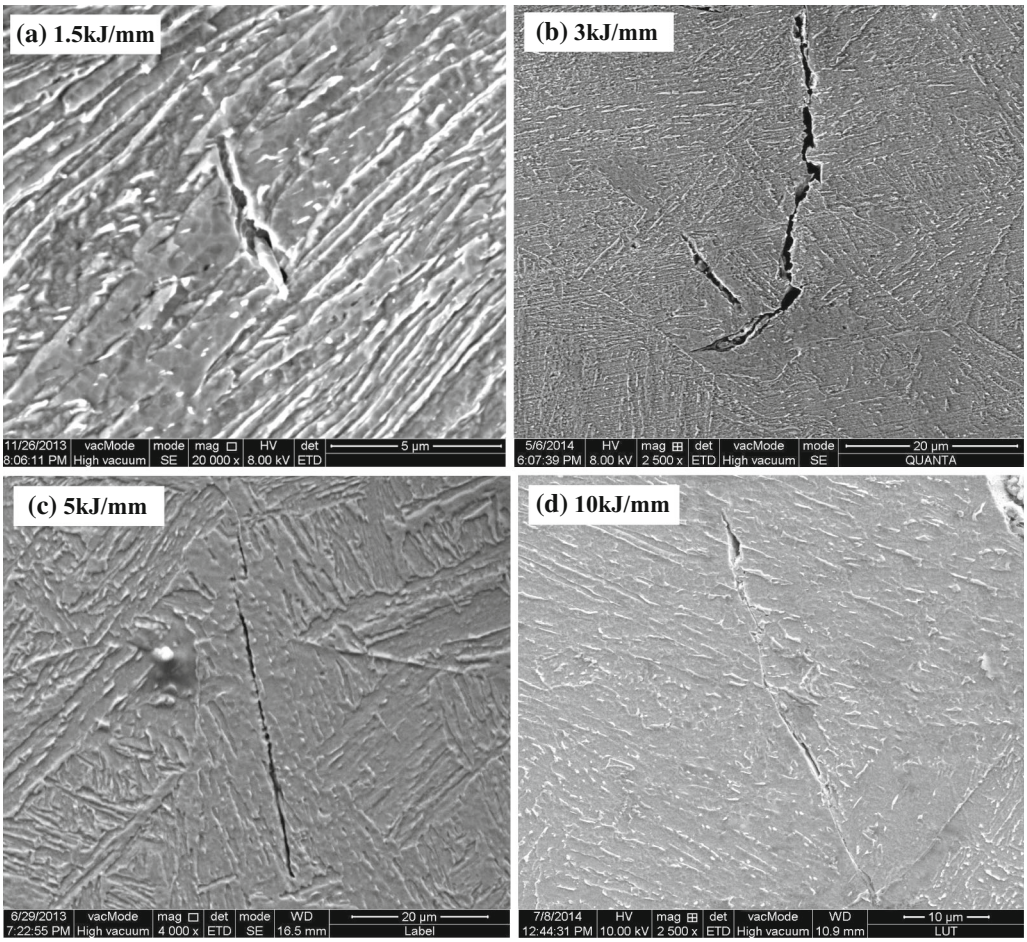


Fig. 26—Packet-sized crack retained in specimens (*a*) 1.5 kJ/mm at 168 K (−105 °C), (*b*) 3 kJ/mm at 168 K (−105 °C), (*c*) 5 kJ/mm at 233 K (−40 °C), (*d*) 10 kJ/cm fractured at 233 K (−40 °C).

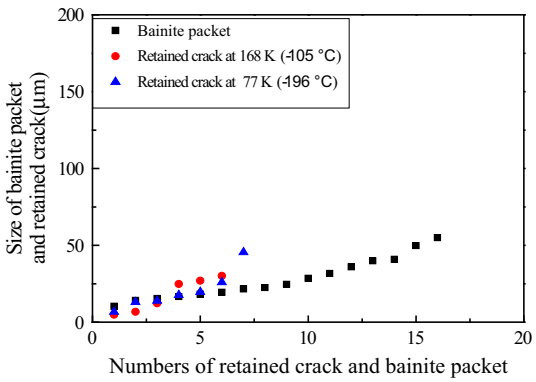


Fig. 27—Measurements of sizes of retained cracks and bainite packets in specimen with welding heat input of 1.5 kJ/mm.

decrease in toughness at a certain low temperature in the lower shelf region, which should be attributed to the increases of the maximum bainite packets due to the increases of the welding heat input. This is the micromechanism of decrease of impact toughness in the lower shelf temperature region with the increasing heat input of welding.

### C. *The Fracture Mechanism and the Toughness in the Transition Region*

In this temperature region at first the crack initiates and propagates in the fibrous mode. At a critical moment, when a cleavage crack is triggered, the fibrous cracking is terminated and transfers to cleavage cracking then the cleavage crack extends throughout the specimen.[23] Thus, in the transition region, a fibrous crack precedes the cleavage fracture, which is initiated and extended until a cleavage cracking is triggered and causes the final fracture. As revealed in Figures 22 and 24 in section D in part III for all specimens with various welding heat inputs, even at different temperatures, the same energy is absorbed for extension of one unit length of a fibrous crack. By comparing Figures 16 and 21, the total absorbed energy for a fractured specimen is determined by the final extension length of the fibrous crack before it is terminated by the cleavage fracture. For example at 193 K (−80 °C), the measured impact energy (in Figure 16) for specimen with heat inputs of 1.5, 3.0, 5.0, and 10.0 kJ/mm is about 250, 60, 15, and 10 J, respectively. These values are correspondingly consistent with the lengths of the fibrous cracks shown in Figures 19 and 21. Figure 17 displays the load–displacement curves. For specimen with heat input of

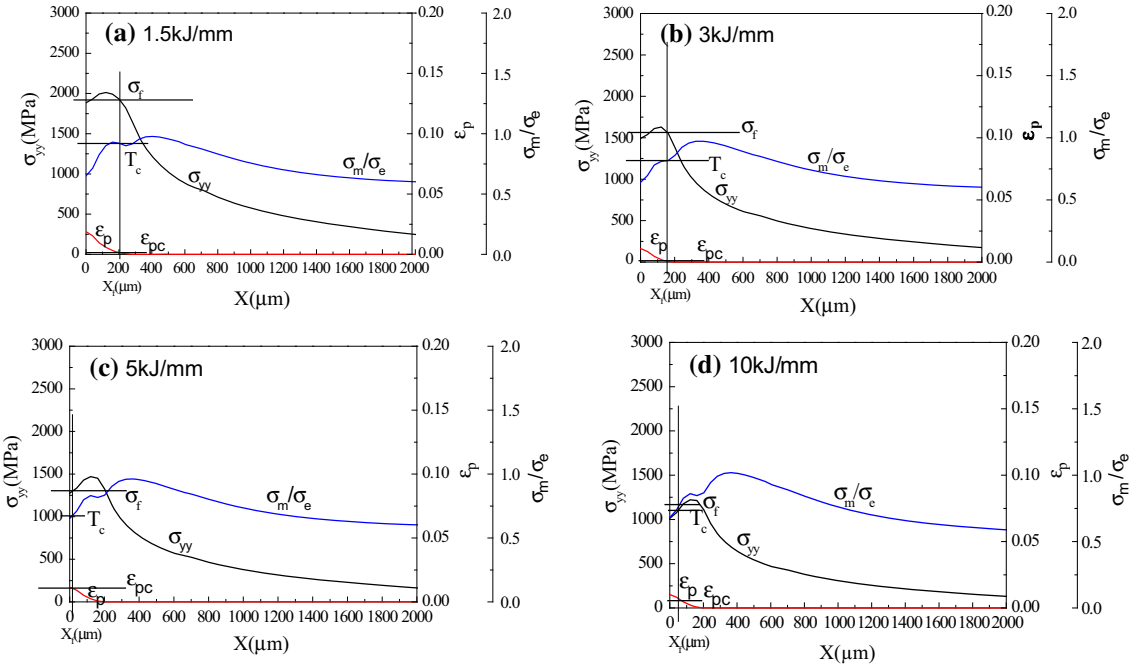


Fig. 28—Stress, strain, and stress triaxiality distributions ahead of the notch for specimen with welding heat input of (*a*) 1.5 kJ/mm, (*b*) 3 kJ/mm, (*c*) 5 kJ/mm, (*d*) 10 kJ/mm at 77 K (−196 °C).

**Table IV. Micro-parameters for Cleavage Fracture at 77 K (−196 °C)**

| Heat Input (kJ/mm) | $a_c$ ($\mu$m) | $E$ (MPa) | $\nu$ | $\sigma_{yd}$ (MPa) | $\sigma_f$ (MPa) | $\varepsilon_{pc}$ | $T_c$ | $Q_c$ ($\sigma_f/\sigma_{yd}$) | $\gamma$ (N/m) |
|---|---|---|---|---|---|---|---|---|---|
| 1.5 | 23.4 | 200,000 | 0.3 | 1190 | 1916 | 0.0041 | 0.92 | 1.61 | 615 |
| 3 | 34.3 | 200,000 | 0.3 | 1096 | 1567 | 0.0008 | 0.82 | 1.43 | 603 |
| 5 | 54.9 | 200,000 | 0.3 | 1005 | 1300 | 0.0105 | 0.68 | 1.29 | 663 |
| 10 | 67.7 | 200,000 | 0.3 | 897 | 1104 | 0.0070 | 0.76 | 1.23 | 590 |

$a_c$: half cleavage facet size around the crack initiation site; $\sigma_{yd}$: dynamic yield strength; $\sigma_f$: local cleavage fracture stress; $\varepsilon_{pc}$: fracture strain; $T_C$: critical stress triaxiality; $Q_c$: critical stress intensification factor; $\gamma$: effective surface energy.

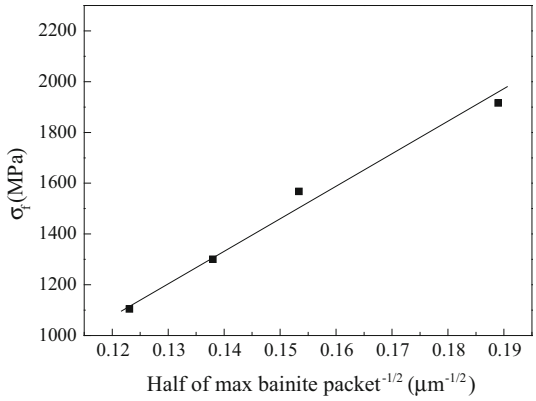


Fig. 29—Plot of local cleavage fracture stress $\sigma_f$ against the square root of the maximum size of bainite packet.

1.5 kJ/mm, a large part of energy is spent in extending the fibrous crack exhibiting in a longer displacement before cleavage cracking. However, for specimen with heat input of 10.0 kJ/mm, the cleavage cracking happens at very early stage of loading without fibrous crack extension. The total absorbed energy is less than 20 J. According to Figure 22, this value is less than the energy spent for a full extension of the stretch zone. It means that the crack initiation energy (spent for SZW) is also very low. Thus, the toughness measured at a certain temperature in the transition region is determined mainly by the length of the fibrous crack *i.e.*, by the moment, earlier or later, the cleavage fracture is triggered. Therefore, the cleavage fracture and the criterion $\sigma_{yy} \geq \sigma_f$ not only determine the toughness measured in the lower shelf region but also have a decisive effect on the toughness in the transition region. The effect of the local cleavage fracture stress $\sigma_f$ and the factors affecting its value in the lower shelf region are available for the transition temperature region. It reveals that the decrease of impact toughness in the CGHAZ in the transition temperature region stems also from the coarsening of bainite packets with the increasing heat input of welding. The higher is the welding heat input, the coarser is the bainite packet, the lower is the $\sigma_f$ (the critical stress intensification factor $Q_c = \sigma_f/\sigma_y$) and

the earlier the cleavage fracture is triggered, the earlier the fibrous cracking is terminated, and the shorter is the fibrous crack length, thus the lower is the impact energy measured. This is the micromechanism of decrease of impact toughness in the transition temperature region in CGHAZ with the increasing heat input of welding.

## V. CONCLUSIONS

Through comprehensive examination of all factors which affect the toughness in a notched impact specimen, the micromechanism of decrease of impact toughness in CGHAZ of the high-strength steel F460 with the increasing heat input of welding can be described as follows:

1. For F460 high-strength steel ship plate, the microstructures in the welding CGHAZ simulated with heat inputs of 1.5, 3.0, 5.0, and 10.0 kJ/mm are evolved from lath martensite, lath bainite, mixture of lath bainite and granular bainite to granular bainite.
2. Increase of welding heat input results in larger grain size of austenite: 164, 225, 282, and 293 $\mu$m and correspondingly to larger bainite packets: 56, 85, 105, and 132 $\mu$m for the four heat input levels. The EBSD map clarifies the trend of raising the proportion of the high degree boundaries by decreasing the heat input is clarified.
3. The crack initiation energy increases with the increase of SZW at a rate of 0.26 J per unit SZW. For all specimens, the maximum of SZW is limited to about 200 to 500 $\mu$m and the corresponding crack initiation energy is about 40 to 60 J.
4. The fibrous crack propagation energy increases with the increasing fibrous crack length. The absorbed energy for unit fibrous crack length (SCL) is the same at a rate of 0.056 J per unit SCL for specimens tested at various temperature and with various welding heat input.
5. The critical event for cleavage fracture is identified as the propagation of the bainite packet-sized crack. The local cleavage fracture stress $\sigma_f$ is determined by the square root of the bainite packet size and it can be measured as the value of the ordinate of the stress distribution curve at the fracture distance $X_f$.
6. With the increasing welding heat input, $\sigma_f$ decreases to 1916, 1567, 1300, and 1104 MPa and the corresponding values of critical values of the stress intensification $Q_c = \sigma_f/\sigma_{yd}$ being 1.61, 1.43, 1.29, and 1.23.
7. Decrease of $\sigma_f$ makes the cleavage fracture easier and decreases the toughness in the lower shelf region. It also makes the termination of the extension of the fibrous crack early and cuts down its length, thus decreases the toughness in the transition temperature region.


## ACKNOWLEDGMENTS

This work was financially supported by Pre-research of National Basic Research Program of China (2014CB660810), National Nature Science Foundation of China (Nos. 51301083, 51265028), and the Rose Willow Outstanding Individual Programs of Lanzhou university of Technology (J201203). EBSD research was supported by ORNL's Shared Research Equipment (ShaRE) User Program, which was sponsored by the Office of Basic Energy Sciences, the U.S. Department of Energy.


## REFERENCES


1. N. McPherson: *Ironmak. Steelmak.*, 2009, vol. 36, pp. 193–200.
2. K. Ichimiya, H. Sumi, and T. Hiral: *JFE Tech. Rep.*, 2008, vol. 11, pp. 7–12.
3. V. Schwinn, J. Bauer, P. Flüss, H.-J. Kirsch, and E. Amoris: *Rev. Métall.*, 2011, vol. 05, pp. 283–94.
4. Y. Nagai, H. Fukami, H. Inoue, A. Date, T. Nakashima, A. Kojima, and T. Adachi: Report No. 90, Nippon Steel, Chiyoda, Tokyo, July 2004.
5. W. Schutz and F. Schroter: *Mater. Sci. Technol.*, 2005, vol. 5, pp. 590–96.
6. L.Y. Lan, X.W. Kong, and Z.Y. Hu: *Philos. Mag. Lett.*, 2014, vol. 94, pp. 764–71.
7. E.F. Nippes and J.P. Balaguer: *Weld. J.*, 1986, vol. 65, pp. 237-s–43-s.
8. J. Neves and A. Loureiro: *J. Mater. Process. Tech*, 2004, vol. 153, pp. 537–43.
9. D. Kaplan and A. Lambert-Perlade: *Rev. Métall.*, 2001, vol. 10, pp. 889–98.
10. M. Shome: *Mater. Sci. Eng. A*, 2007, vol. 445, pp. 454–60.
11. E.F. Nippes and W.F. Savage: *Weld. J*, 1949, vol. 28, pp. 534–46.
12. X. Li, X. Ma, and S.V. Subramanian: *Mater. Sci. Eng.*, 2014, vol. 616, pp. 141–47.
13. K. Banerjee, M. Militzer, M. Perez, and X. Wang: *Metall. Mater. Trans. A*, 2010, vol. 41A, pp. 3161–72.
14. L. Zhang and T. Kannengiesser: *Mater. Sci. Eng.*, 2014, vol. 613, pp. 326–35.
15. H.Q. Yan, K.M. Wu, and H.H. Wang: *Sci. Technol. Weld. Join.*, 2014, vol. 19, pp. 355–60.
16. D.S. Liu, Q.L. Li, and T. Emi: *Metall. Mater. Trans. A*, 2011, vol. 42A, pp. 1349–61.
17. D.S. Liu, B.G. Cheng, and M. Luo: *ISIJ Int.*, 2011, vol. 4, pp. 603–11.
18. M. Shi, P. Zhang, and C. Wang: *ISIJ Int.*, 2014, vol. 54, pp. 932–37.
19. L. Yu, H.H. Wang, and T.P. Hou: *Sci. Technol. Weld. Joi.*, 2014, vol. 19, pp. 708–14.
20. G. Spanos, D. Moon, R. Fonda, E. Menon, and A. Fox: *Metall. Mater. Trans. A*, 2001, vol. 32A, pp. 3043–54.
21. R. Cao, W. Feng, Y. Peng, W.S. Du, Z.L. Tian, and J.H. Chen: *Metall. Mater. Trans. A*, 2010, vol. 41A, pp. 631–42.
22. D.S. Liu, B.G. Cheng, and M. Luo: *Acta Metall. Sin.*, 2011, vol. 10, pp. 1233–40.
23. J.H. Chen and R. Cao: *Micromechanism of Cleavage Fracture of Metals: A Comprehensive Microphysical Model for Cleavage Cracking in Metals*, Elsevier, Oxford, U.K., 2014, ISBN: 9780128007655.
24. N.N. Rykalin: Calculation of Heat Flow in Welding, IIW Doc. 212-350-74, 1974.
25. E. Smith: *Int. J. Fract.*, 1968, vol. 94, pp. 33–49.